Two-axis control of a singlet–triplet qubit with an integrated micromagnet

Xian Wu[a], D. R. Ward[a], J. R. Prance[b], Dohun Kim[a], John King Gamble[a], R. T. Mohr[a], Zhan Shi[a], D. E. Savage[c], M. G. Lagally[c], Mark Friesen[a], S. N. Coppersmith[a,1], and M. A. Eriksson[a,1]

Departments of [a]Physics and [c]Materials Science and Engineering, University of Wisconsin, Madison, WI 53706; and [b]Department of Physics, Lancaster University, Lancaster LA1 4YB, United Kingdom

Contributed by S. N. Coppersmith, June 30, 2014 (sent for review March 19, 2014)

The qubit is the fundamental building block of a quantum computer. We fabricate a qubit in a silicon double-quantum dot with an integrated micromagnet in which the qubit basis states are the singlet state and the spin-zero triplet state of two electrons. Because of the micromagnet, the magnetic field difference ΔB between the two sides of the double dot is large enough to enable the achievement of coherent rotation of the qubit's Bloch vector around two different axes of the Bloch sphere. By measuring the decay of the quantum oscillations, the inhomogeneous spin coherence time T_2^* is determined. By measuring T_2^* at many different values of the exchange coupling J and at two different values of ΔB, we provide evidence that the micromagnet does not limit decoherence, with the dominant limits on T_2^* arising from charge noise and from coupling to nuclear spins.

semiconductor spin qubit | quantum nanoelectronics

Fabricating qubits composed of electrons in semiconductor quantum dots is a promising approach for the development of a large-scale quantum computer because of the approach's potential for scalability and for integrability with classical electronics. Much recent progress has been made, and spin manipulation has been demonstrated in systems of two (1–5), three (6, 7), and four (8) quantum dots. A great deal of attention has focused on the singlet–triplet qubit in quantum dots (1, 2, 9–18), which consists of the $S_z = 0$ subspace of two electrons, for which the basis can be chosen to be a singlet and a triplet state. Full two-axis control on the Bloch sphere is achieved by electrical gating in the presence of a magnetic field difference ΔB between the two dots. In previous experiments (2, 9–14), ΔB arises from coupling to nuclear spins in the material, and slow fluctuations in these nuclear fields lead to inhomogeneous decoherence times that, without special nuclear state preparation, typically are shorter than the period of the quantum oscillations. In III–V materials, ΔB is large, so fast oscillation periods of order 10 ns are achievable, but the inhomogeneous dephasing time is also ~10 ns, so that oscillations from ΔB are overdamped, ending before a complete cycle is observed (2). The fluctuations of the nuclear spin bath can be mitigated to some extent (10), but inhomogeneous dephasing times in III–V materials are short enough that high-fidelity control is still very challenging. Coupling to nuclear spins in silicon is substantially weaker, leading to longer coherence times, but also smaller field differences and hence slower quantum oscillations (14, 19).

Here, we report the operation of a singlet–triplet qubit in which the magnetic field difference ΔB between the dots is imposed by an external micromagnet (20, 21). Because the field from the micromagnet is stable in time, a large ΔB can be imposed without creating inhomogeneous dephasing. We present data demonstrating underdamped quantum oscillations, and, by investigating a variety of voltage configurations and two ΔB configurations, we show that the micromagnet indeed increases ΔB without significantly increasing inhomogeneous dephasing rates induced by coupling to nuclear spins.

A top view of the double-quantum dot device, which is fabricated in a Si/SiGe heterostructure, is shown in Fig. 1*A*; fabrication techniques are discussed in *Materials and Methods*, and an optical image of the micromagnet can be found in *SI Appendix*. The charge occupation of the two sides of the double dot is determined by measuring the current through a quantum point contact (QPC) next to one of the dots, as shown in Fig. 1*A*. Fig. 1*B* shows a charge stability diagram, obtained by measuring the current through the QPC as a function of gate voltages on the left plunger (LP) and right plunger (RP); the number of electrons on each side of the dot is labeled. The qubit manipulations are performed in the (1, 1) region (detuning $\varepsilon > 0$), and initialization and readout are carried out in the (0, 2) region ($\varepsilon < 0$). Fig. 1*C* shows the energy-level diagram at small but nonzero magnetic field. The three triplet states $T_- = |\downarrow\downarrow\rangle$, $T_0 = (|\uparrow\downarrow\rangle + |\downarrow\uparrow\rangle)/\sqrt{2}$, and $T_+ = |\uparrow\uparrow\rangle$ are split from each other by the Zeeman energy $E_Z = g\mu_B B_{ave}$, where g is the gyromagnetic ratio, μ_B is the Bohr magneton, and B_{ave} is the average of the total magnetic field. A difference in the transverse magnetic fields on the dots, either from the external micromagnet or from nuclear hyperfine fields, mixes the singlet S and triplet T_- states and turns the S-T_- crossing into an anticrossing. This avoided crossing enables the observation of a spin funnel where the S-T_- mixing is fast (2) as well as quantum oscillations between S and T_- (22). The spin funnel is shown in Fig. 1*E*, and the S-T_- oscillations are shown in Fig. 1 *F* and *G*. The applied pulse in Fig. 1*E* is a simple one-stage pulse along the detuning direction with fixed amplitude (shown in Fig. 1*C*, *Inset*), repeated at a rate of 33 kHz, which is slow enough for spin relaxation to reinitialize to the singlet before application of the next pulse (23,

Significance

Qubits, the quantum-mechanical analog of classical bits, are the fundamental building blocks of quantum computers, which have the potential to solve some problems that are intractable using classical computation. This paper reports the fabrication and operation of a qubit in a double-quantum dot in a silicon/silicon–germanium (Si/SiGe) heterostructure in which the qubit states are singlet and triplet states of two electrons. The significant advance over previous work is that a proximal micromagnet is used to create a large local magnetic field difference between the two sides of the quantum dot, which increases the manipulability significantly without introducing measurable noise.

Author contributions: X.W., D.R.W., J.R.P., D.K., J.K.G., R.T.M., Z.S., M.F., S.N.C., and M.A.E. designed research; X.W., D.R.W., J.R.P., D.K., J.K.G., R.T.M., Z.S., D.E.S., M.G.L., M.F., S.N.C., and M.A.E. performed research; D.R.W. contributed new reagents/analytic tools; D.R.W., D.E.S., and M.G.L. fabricated the sample; X.W., M.F., S.N.C., and M.A.E. analyzed data; and X.W., M.F., S.N.C., and M.A.E. wrote the paper, with input from all the authors.

The authors declare no conflict of interest.

[1] To whom correspondence may be addressed. Email: snc@physics.wisc.edu or maeriksson@wisc.edu.

This article contains supporting information online at www.pnas.org/lookup/suppl/doi:10.1073/pnas.1412230111/-/DCSupplemental.

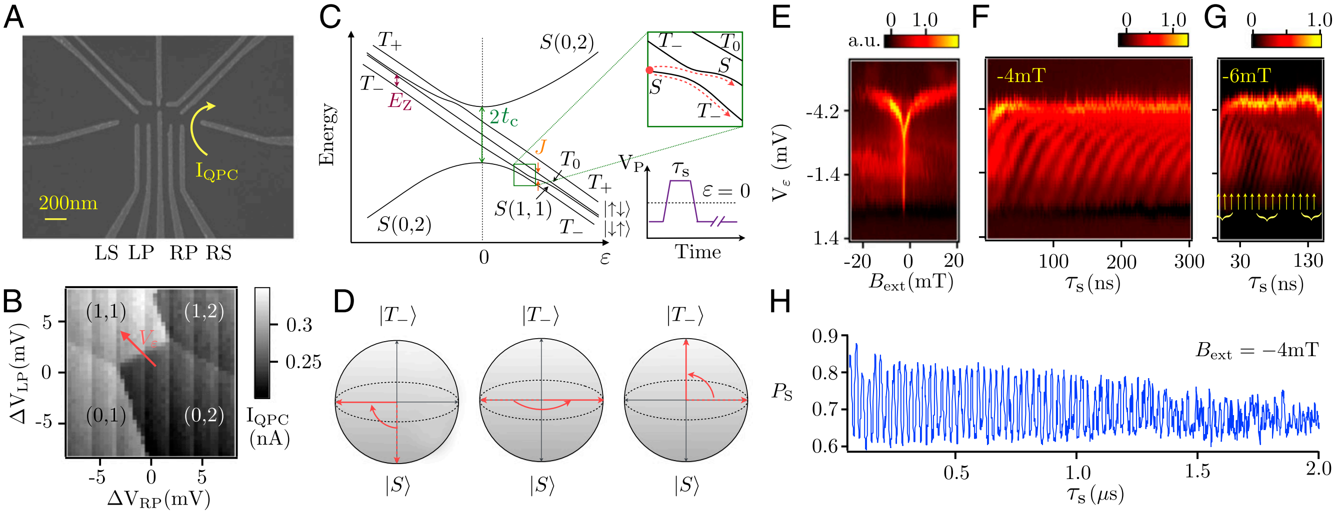

Fig. 1. (*A*) Scanning electron micrograph of a device identical to the one used in the experiment before deposition of the gate dielectric and accumulation gates. An optical image of a complete device showing the micromagnet is included in *SI Appendix*. Gates labeled left side (LS) and right side (RS) are used for fast pulsing. The curved arrow shows the current path through the QPC used as a charge sensor. (*B*) I_{QPC} measured as a function of V_{LP} and V_{RP} yields the double-dot charge stability diagram. Electron numbers in the left and right dot are indicated on the diagram. The red arrow denotes the direction in gate voltage space $V_\varepsilon = \sqrt{\Delta V_{LP}^2 + \Delta V_{RP}^2}$ that changes the detuning ε between the quantum dots. (*C*) Schematic energy diagram near the (0, 2) to (1, 1) charge transition, showing energies of singlet S and triplet T states as functions of ε. The exchange energy splitting J between S and T_0, the Zeeman splitting E_Z between T_- and T_0, and the tunnel coupling t_c are also shown. At large ε, in the presence of a field difference between the two dots, S and T_0 mix, and the corresponding energy eigenstates are $|\uparrow\downarrow\rangle$ and $|\downarrow\uparrow\rangle$. At small ε, the small transverse field from the micromagnet and the nuclear fields turns the S-T_- crossing into an anticrossing (zoom in). Pulsing through this anticrossing with intermediate velocity transforms S into a superposition of S and T_-, leading to Landau–Stückelberg–Zener oscillations at the frequency corresponding to the S-T_- energy difference (22). The pulse used to observe the spin funnel and S-T_- oscillations shown in *E* is also shown, where the pulse voltage V_P is applied along the detuning axis. (*D*) Bloch sphere representation of π rotation of S and T_- states with 50% initialization into each state. (*E*) Spin funnel (2) measurement of the location of the S-T_- anticrossing as a function of external magnetic field B_{ext} and V_ε. The data were acquired by sweeping along the detuning direction with the pulse on, with the vertical axis reporting the value of the detuning at the base of the pulse. The spin funnel occurs when S-T_- mixing is fast, which locates the relevant anticrossing. (*F* and *G*) S-T_- oscillations acquired at different external B fields. The oscillation frequency increases with increasing B_{ext}. The slower oscillations in *G* with period ~80 ns and labeled with the curly brackets are S-T_0 oscillations, which are investigated in more detail in Figs. 2 and 3. The S-T_- oscillations in *G* are labeled with arrows. (*H*) Singlet probability as a function of pulse duration τ_s at external magnetic field B = −4 mT and base detuning $V_\varepsilon \simeq -2.8$ mV.

24). The lever arm α, the conversion between detuning energy ε and gate voltage V_ε, is 35.4 μeV/mV. See *SI Appendix* for methods used to extract α and convert the measured QPC current to the probability of being in the S state at the end of the applied pulse. The spin funnel is obtained by sweeping along the detuning direction (i.e., sweeping V_ε) with the pulse on, and stepping the external magnetic field B_{ext}. When the pulse tip reaches the S-T_- anticrossing, a strong resonance signal is observed, corresponding to strong mixing of S-T_- states. Because right at the anticrossing $E_Z \simeq J$, we can map out J at small ε by sweeping the magnetic field. The center of the spin funnel occurs when the applied field cancels out the average field from the micromagnet, which indicates $B_{ave} \simeq 2.5$ mT. The tunnel coupling $t_c \sim 3.4$ μeV is estimated from the dependence of the location of the spin funnel on magnetic field (2). The pulse rise time of 10 ns ensures nearly adiabatic passage over the $S(0, 2)$ to $S(1, 1)$ anticrossing, with a nonadiabatic transition probability <0.1% (25).

By increasing the rise time of the pulse, so that it is slower than that used to observe the spin funnel, the voltage pulse can be used to cause S to evolve into a superposition of the S and T_- states. In this case, the pulse remains adiabatic with respect to the $S(0, 2)$–$S(1, 1)$ anticrossing; it is, however, only quasi-adiabatic with respect to the S-T_- anticrossing, enabling use of the Landau–Zener mechanism to initialize a superposition between states S and T_- (Fig. 1*C*, *Inset*) (22, 26–28). Because the voltage pulse takes these states to larger detuning, an energy difference arises between the pair of states, and there is a relative phase accumulation between them. The return pulse leads to quantum interference between these two states and to oscillations in the charge occupation as a function of the acquired phase. Fig. 1*D* illustrates the ideal case, in which the rising edge of the pulse transforms S into an equal superposition of S and T_-, followed by accumulation of a relative phase difference of π after pulse duration τ_S. Fig. 1*F* shows S-T_- oscillations at $B_{ext} = -4$ mT, obtained by applying a pulse with a rise time of 45 ns. Fig. 1*H* reports a line scan of the singlet probability for S-T_- oscillations measured at $B_{ext} = -4$ mT; for this measurement, the tip of the voltage pulse reaches large enough detuning that E_{ST_-} is essentially constant and independent of detuning. From this data we extract a dephasing time of 1.7 μs by fitting the oscillation amplitude to a Gaussian decay function of the pulse duration τ_S. The S-T_- oscillations observed here are longer-lived than those observed in GaAs (22), presumably in part because Si has weaker hyperfine fields (29). However, the visibility here is similar to that in GaAs, indicating that decoherence is still important in limiting the ability to tune the pulse rise time to achieve equal amplitude in the S and T_- branches of the Landau–Zener beam splitter (22, 26–28). Fig. 1*G* shows a similar measurement for which we used a slightly faster (16 ns) rise time for the pulse, the effect of which is to increase the overlap of the wavefunction with the singlet state S; as a result, both S-T_- oscillations and S-T_0 oscillations are visible in this plot, which was acquired at $B_{ext} = -6$ mT. The faster oscillations with period 10 ns, marked with the small arrows in Fig. 1*G*, are the S-T_- oscillations. The slower oscillations, marked with the curly brackets, are the S-T_0 oscillations. As we discuss below, these latter oscillations can be made dominant by further modifications of the manipulation pulse, and for these oscillations the micromagnet plays a critical role in enhancing the rotation rate on the S-T_0 Bloch sphere.

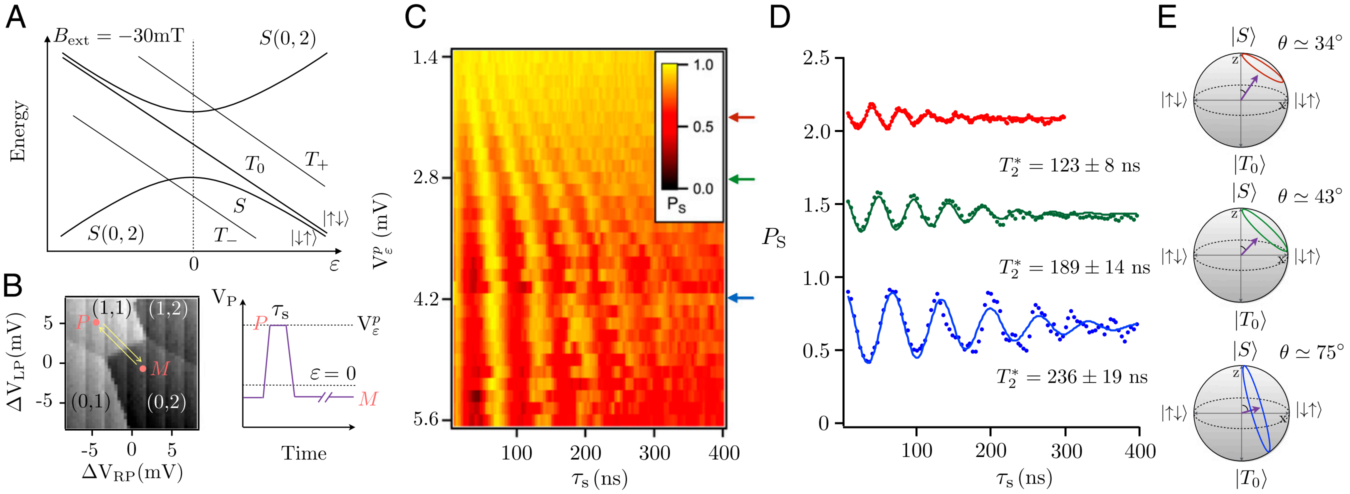

Fig. 2. (*A*) Schematic energy level diagram near the (0, 2)–(1, 1) charge transition at external field $B_{\rm ext} = -30$ mT. (*B*) Pulse sequence used to observe *S*-T_0 oscillations. Starting at point M in the *S*(0, 2) ground state, a fast adiabatic pulse into (1, 1) is applied [it is adiabatic for the *S*(0, 2)–*S*(1, 1) anticrossing and sudden for the *S*(1, 1)-T_0 anticrossing], to point P, where the exchange coupling *J* is comparable to or less than *h*, the energy from the magnetic field difference. The speed and axis of the rotation on the Bloch sphere during the pulse of duration τ_s depend on both *J* and *h*. Readout is performed by reversing the fast adiabatic pulse, which converts *S*(1, 1) to *S*(0, 2) but does not change the charge configuration of T_0. (*C*) Probability P_S of being in state *S* as a function of the detuning voltage at the pulse tip, $V^{\rm p}_\varepsilon$, and the pulse duration τ_s. Here, the measurement point M in the (0, 2) charge state is fixed while $V^{\rm p}_\varepsilon$ and τ_s are varied. (*D*) P_S as a function of τ_s, extracted from the data in *C* at three different values of V_ε. Each trace is fit to the product of a cosine and a Gaussian (30, 31), with amplitude, frequency, phase, and decay time as free parameters (solid curves). The decay time T_2^* is listed for each trace. Each trace is offset by 0.6 for clarity. (*E*) Bloch spheres showing the rotations corresponding to each trace in *D*. The angle θ between the rotation axis and the *z* axis is labeled for each case.

We investigate the *S*-T_0 oscillations, which correspond to a gate rotation of the *S*-T_0 qubit, in more detail by changing the applied magnetic field $B_{\rm ext}$ to −30 mT, and by working with faster pulse rise times. Here the *S*-T_- anticrossing occurs at negative ε, as shown in Fig. 2*A*, making it easier to pulse through that anticrossing quickly enough so that the state remains *S*. In this situation, the relevant Hamiltonian *H* for $\varepsilon > 0$, in the *S*-T_0 basis, is

$$H = \begin{bmatrix} -J(\epsilon) & h/2 \\ h/2 & 0 \end{bmatrix}. \qquad \textbf{[1]}$$

Here, *J* is the exchange coupling and $h = g\mu_{\rm B}\Delta B$ is the energy contribution from the magnetic field difference. The angle θ between the rotation axis and the *z* axis of the Bloch sphere satisfies $\tan\theta = h/J$, and the rotation angular frequency $\omega = \sqrt{h^2 + J^2}/\hbar$. Both θ and ω depend on ε, because *J* varies with ε.

Rotations around the *x* axis of the Bloch sphere (the "Δ*B* gate") are implemented using the simple one stage pulse shown in Fig. 2*B*, starting from point M in the (0, 2) charge state. The pulse rise time of a few nanoseconds is slow enough that the pulse is adiabatic through the *S*(0, 2) to *S*(1, 1) anticrossing. As ε increases, the eigenstates transition from *S*(1, 1) and T_0 to other combinations of $|\uparrow\downarrow\rangle$ and $|\downarrow\uparrow\rangle$, and in the limit of $\varepsilon \to \infty$, the eigenstates become $|\uparrow\downarrow\rangle$ and $|\downarrow\uparrow\rangle$. The voltage pulse applied is sudden with respect to this transition in the energy eigenstates, so that immediately following the rising edge of the pulse the system remains in *S*(1, 1). At large detuning, $J \leq h$, and *S*-T_0 oscillations are observed following the returning edge of the pulse. These oscillations arise from the *x* component of the rotation axis and have a rotation rate that is largely determined by the magnitude of *h*. Fig. 2*C* shows the singlet probability P_S plotted as a function of the detuning voltage at the pulse tip, $V^{\rm p}_\varepsilon$, and pulse duration τ_S. The data in the top one-third of the figure were acquired with a pulse rise time of 2.5 ns, and the data shown in the bottom two-thirds of the figure were acquired using a 5-ns rise time. As is clear from Fig. 2 *C* and *D*, *J* decreases as ε increases, so the oscillation angular frequency becomes smaller and approaches $h/\hbar$ as $J \to 0$. The visibility of the oscillations is largest at large $V^{\rm p}_\varepsilon$, because in that regime the rotation axis is closest to the *x* axis, as shown in Fig. 2*E*. By fitting traces from Fig. 2*C* to the product of a cosine and a Gaussian (30), we extract the inhomogeneous dephasing time T_2^* as a function of ε. Based on the rotation period at large ε, we estimate $h \sim 60.5$ neV, which corresponds to an X-rotation rate of 14 MHz. The rotation rate we observe here is much faster than the X-rotation rate achievable without micromagnets in Si, which is ∼460 kHz (14); micromagnets closer to the quantum dots offer the potential for even faster rotation rates than those reported here. Using feedback to prepare the nuclear spins in GaAs quantum dots, X-rotation rates of 30 MHz have been reported (18), comparable but slightly faster than the rates we achieve here without such preparation.

Fig. 3 shows oscillations around the *z* axis of the Bloch sphere, obtained by applying the exchange pulse sequence pioneered in (2). Starting from point M in *S*(0, 2), we first ramp from M to N at a rate that ensures fast passage through the *S*(0, 2)-T_- anticrossing, converting the state to *S*(1, 1), and then ramp adiabatically from N to P, which initializes to the ground state in the $J < h$ region. The pulse from P to E increases *J* suddenly so that it is comparable to or bigger than *h*, so that the rotation axis is close to the *z* axis of the Bloch sphere. Readout is performed by reversing the ramps, which projects $|\downarrow\uparrow\rangle$ into the *S*(2, 0) state, enabling readout. Fig. 3*C* shows the singlet probability P_S as a function of τ_S and the detuning of the exchange pulse $V^{\rm ex}_\varepsilon$ (point E in Fig. 3*B*) in a range of ε where $J \gtrsim h$. As $V^{\rm ex}_\varepsilon$ decreases, the oscillation frequency increases, because *J* is increasing. The oscillation visibility also increases as the rotation axis moves toward the *z* axis, as shown in Fig. 3 *D* and *E*. The inhomogeneous dephasing time T_2^*, extracted by fitting the time dependence of P_S in Fig. 3*D* to the product of a Gaussian and a cosine function, decreases as *J* increases, which we argue is evidence that charge noise is limiting coherence in this regime (see below and Fig. 4).

We also implemented both the Δ*B* and exchange gate sequences after performing a different cycling of the external magnetic field, which resulted in a different value of Δ*B*, corresponding to $h \simeq 32$ neV. The results obtained are qualitatively consistent

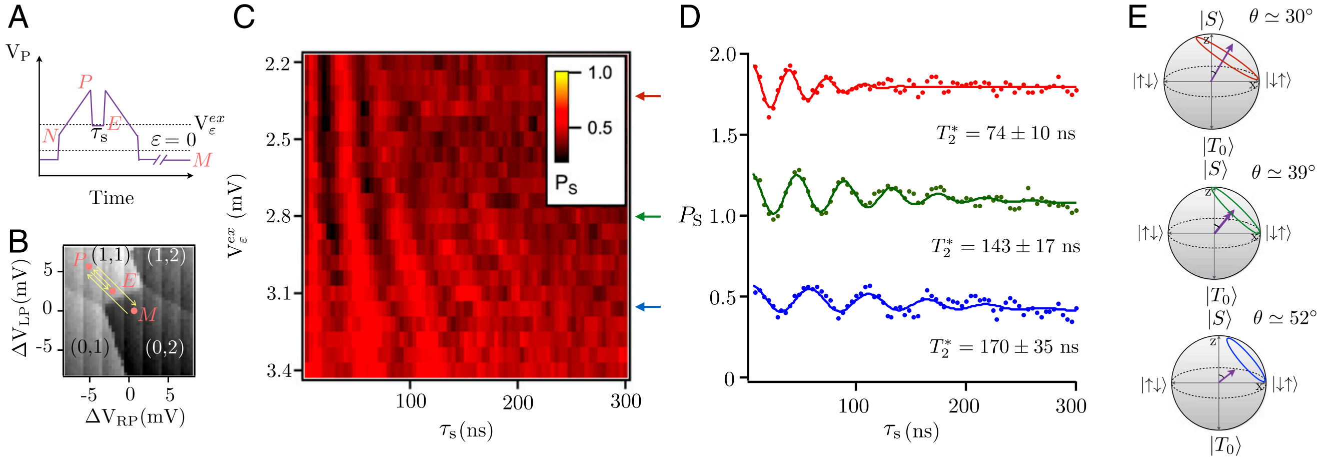

Fig. 3. (*A* and *B*) Pulse sequence used to observe *S*-T_0 oscillations when $J > h$. We initialize into the *S*(1, 1) state by preparing the *S*(0, 2) ground state at point M and ramping adiabatically through the (0, 2)–(1, 1)*S* anticrossing to an intermediate point N and then to P, where the singlet and triplet states are no longer energy eigenstates. Decreasing ε suddenly brings the state nonadiabatically to a value of the detuning where *J* is comparable or greater than *h*, inducing coherent rotations. The Bloch vector rotates around the new axis for a time τ_s. Reversing the sequence of ramps projects the state into *S*(0, 2) for readout. (*C*) Probability P_S of observing the singlet as a function of the detuning voltage of the exchange pulse V_ε^{ex} and pulse duration τ_s with the measurement point M fixed in the (0, 2) charge state. (*D*) P_S as a function of τ_s, extracted from the data in *C* at three different values of V_ε^{ex}. Each trace is offset by 0.7 for clarity. Solid curves are fits to the product of a cosine and a Gaussian (30), with amplitude, frequency, phase, and decay time as free parameters. (*E*) Bloch spheres showing rotations around the axes corresponding to each trace in *D*. The angle θ between the rotation axis and the *z* axis is labeled for each case.

with those shown in Figs. 2 and 3 (data shown in the *SI Appendix*, Fig. S3).

We now present evidence that the inhomogeneous dephasing is dominated by detuning noise and by fluctuating nuclear fields, and that it does not depend on the field from the micromagnet. Following ref. 18, we write $1/T_2^* = \sqrt{\langle(\delta E_{tot})^2\rangle}/(\sqrt{2}\hbar)$, where $\delta E_{tot} = \delta J(\partial E_{tot}/\partial J) + \delta h(\partial E_{tot}/\partial h)$, with δE_{tot} the fluctuation in E_{tot}, δJ the fluctuation in *J*, and δh the fluctuation in *h*. We assume that the fluctuations in *h* and *J* are uncorrelated. If fluctuations in *J* are dominated by fluctuations in the detuning, $\delta\varepsilon$, then $\delta J \sim \delta\varepsilon(dJ/d\varepsilon)$, and if fluctuations in *h* are dominated by nuclear fields, then δh is independent of ε, leading to

$$\sqrt{2}\hbar T_2^{*-1} = \left(\left(\frac{J}{E_{tot}}\frac{dJ}{d\varepsilon}\delta\varepsilon_{rms}\right)^2 + \left(\frac{h}{E_{tot}}\delta h_{rms}\right)^2\right)^{\frac{1}{2}}, \qquad [2]$$

with $\delta\varepsilon_{rms}$ and δh_{rms} both independent of E_{tot} as well as *h*. We use the measured E_{tot} vs. ε to extract $J(\varepsilon)$, which is well-described by an exponential, $J(\varepsilon) \simeq J_0\exp(-\varepsilon/\varepsilon_0)$, consistent with ref. 18 in the same regime (*SI Appendix*). In Fig. 4 we fit T_2^* using the experimentally determined $dJ/d\varepsilon$, the measured E_{tot}, and constant values $\delta\varepsilon_{rms} = 6.4 \pm 0.1$ μeV and $\delta h_{rms} = 4.2 \pm 0.1$ neV. The fit is good, and the values of $\delta\varepsilon_{rms}$ and δh_{rms} agree well with previous reports of charge noise and fluctuations in the nuclear field in similar devices and materials (14, 29, 30, 32–34). Fig. 4 *Inset*, which shows data obtained at a larger *h*, demonstrates that T_2^* is well-described by Eq. **2** with the same $\delta\varepsilon_{rms}$ and δh_{rms}, providing evidence that changing the magnetization of the micromagnet does not significantly affect the qubit decoherence. Eq. **2** and Fig. 4 also make it clear that T_2^* is larger for larger detunings, because charge noise has much less effect away from the primary anticrossing.

In summary, we have demonstrated coherent rotations of the quantum state of a singlet–triplet qubit around two different directions of the Bloch sphere. Measurements of the inhomogeneous dephasing time at a variety of exchange couplings and two different field differences demonstrate that using an external micromagnet yields a large increase in the rotation rate around one axis on the Bloch sphere without inducing significant decoherence. Because the materials fabrication techniques are similar for both quantum dot-based qubits and donor-based qubits in semiconductors (35), it is reasonable to expect micromagnets also should be

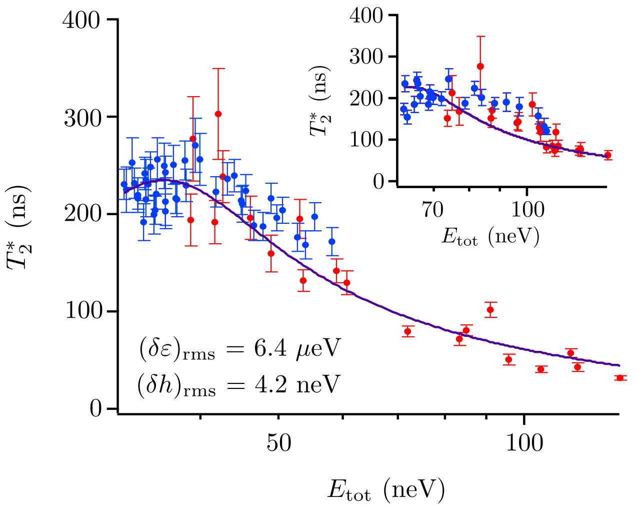

Fig. 4. Dependence of the inhomogeneous dephasing time T_2^* on rotation energy $E_{tot} = \sqrt{J^2 + h^2}$, where *J* is the exchange coupling and *h* is the energy corresponding to the magnetic field difference between the dots. (*Inset*) Plot of the extracted values of T_2^* for $h \simeq 60.5$ neV. Red data points are T_2^* values obtained using the exchange pulse sequence (Fig. 3), and blue data points are T_2^* values obtained using the ΔB pulse (Fig. 2). Main panel: T_2^* plotted vs. E_{tot} for $h \simeq 32$ neV, extracted from data shown in *SI Appendix*, Fig. S3. Red data points are obtained using the exchange pulse sequence (*SI Appendix*, Fig. S3*B*), and blue data points are obtained using the ΔB pulse (*SI Appendix*, Fig. S3*A*). The solid lines in the main panel and in *Inset* are plots of Eq. **2** with the same values of $\delta\varepsilon$, the rms fluctuation in the detuning, and δh, the rms fluctuation of the magnetic field difference, which were obtained by fitting the data for T_2^* as function of E_{tot} at $h \simeq 32$ neV to Eq. **2**. The good agreement of the same form with both data sets is strong evidence that the inhomogeneous dephasing is dominated by charge noise and hyperfine fields and does not depend on the magnetization of the micromagnet.

applicable to donor-based spin qubits (36–38). Micromagnets allow a difference in magnetic field to be generated between pairs of dots that does not depend on nuclear spins, and thus offer a promising path toward fast manipulation in materials with small concentrations of nuclear spins, including both natural Si and isotopically enriched ^{28}Si.

Materials and Methods

All measurements reported in this manuscript were made on a double-quantum dot device fabricated in an undoped Si/Si$_{0.72}$Ge$_{0.28}$ heterostructure with a 12-nm-thick Si quantum well located 32 nm below the heterostructure surface. The double-quantum dot is defined using two layers of electrostatic gates (39–44). The lower layer of depletion gates is shown in Fig. 1*A*. The upper and lower layer of gates are separated by 80 nm of Al$_2$O$_3$ deposited via atomic layer deposition. The upper layer of gates is positively biased to accumulate a 2D electron gas in the Si well. The micromagnet, a rectangular thin film of cobalt, is deposited via electron-beam evaporation on top of the gate structure, 1.78 μm from the double-dot region (*SI Appendix*). A uniform in-plane magnetic field B_{ext} is applied, and cycling B_{ext} to relatively large values is used to change the magnetization of the micromagnet. All measurements were made in a dilution refrigerator with an electron temperature of ~120 mK, as determined using the method of ref. 45.

ACKNOWLEDGMENTS. We thank M. Rzchowski for help in characterizing cobalt films, and acknowledge useful correspondence with W. Coish and F. Beaudoin. This work was supported in part by Army Research Office Grant W911NF-12-0607; National Science Foundation (NSF) Grants DMR-1206915 and PHY-1104660; and the Department of Defense. The views and conclusions contained in this document are those of the authors and should not be interpreted as representing the official policies, either expressly or implied, of the US Government. Development and maintenance of growth facilities used for fabricating samples is supported by Department of Energy Grant DE-FG02-03ER46028, and nanopatterning made use of NSF-supported shared facilities (DMR-1121288).

1. Levy J (2002) Universal quantum computation with spin-1/2 pairs and Heisenberg exchange. *Phys Rev Lett* 89(14):147902.
2. Petta JR, et al. (2005) Coherent manipulation of coupled electron spins in semiconductor quantum dots. *Science* 309(5744):2180–2184.
3. Nowack KC, et al. (2011) Single-shot correlations and two-qubit gate of solid-state spins. *Science* 333(6047):1269–1272.
4. Shi Z, et al. (2014) Fast coherent manipulation of three-electron states in a double quantum dot. *Nat Commun* 5:3020.
5. Kim D, et al. (2014) Quantum control and process tomography of a semiconductor quantum dot hybrid qubit. *Nature* 511:70–74.
6. Gaudreau L, et al. (2012) Coherent control of three-spin states in a triple quantum dot. *Nat Phys* 8:54–58.
7. Medford J, et al. (2013) Self-consistent measurement and state tomography of an exchange-only spin qubit. *Nat Nanotechnol* 8(9):654–659.
8. Shulman MD, et al. (2012) Demonstration of entanglement of electrostatically coupled singlet-triplet qubits. *Science* 336(6078):202–205.
9. Reilly DJ, et al. (2008) Suppressing spin qubit dephasing by nuclear state preparation. *Science* 321(5890):817–821.
10. Foletti S, Bluhm H, Mahalu D, Umansky V, Yacoby A (2009) Universal quantum control of two-electron spin quantum bits using dynamic nuclear polarization. *Nat Phys* 5:903–908.
11. Barthel C, Reilly DJ, Marcus CM, Hanson MP, Gossard AC (2009) Rapid single-shot measurement of a singlet-triplet qubit. *Phys Rev Lett* 103(16):160503.
12. Barthel C, Medford J, Marcus CM, Hanson MP, Gossard AC (2010) Interlaced dynamical decoupling and coherent operation of a singlet-triplet qubit. *Phys Rev Lett* 105(26):266808.
13. Bluhm H, et al. (2011) Dephasing time of GaAs electron-spin qubits coupled to a nuclear bath exceeding 200μs. *Nat Phys* 7:109–113.
14. Maune BM, et al. (2012) Coherent singlet-triplet oscillations in a silicon-based double quantum dot. *Nature* 481(7381):344–347.
15. Shi Z, et al. (2011) Tunable singlet-triplet splitting in a few-electron Si/SiGe quantum dot. *Appl Phys Lett* 99(23):233108.
16. Otsuka T, Sugihara Y, Yoneda J, Katsumoto S, Tarucha S (2012) Detection of spin polarization utilizing singlet and triplet states in a single-lead quantum dot. *Phys Rev B* 86(8):081308.
17. Studenikin SA, et al. (2012) Quantum interference between three two-spin states in a double quantum dot. *Phys Rev Lett* 108(22):226802.
18. Dial OE, et al. (2013) Charge noise spectroscopy using coherent exchange oscillations in a singlet-triplet qubit. *Phys Rev Lett* 110(14):146804.
19. Zwanenburg FA, et al. (2013) Silicon quantum electronics. *Rev Mod Phys* 85(3):961–1019.
20. Pioro-Ladrière M, Tokura Y, Obata T, Kubo T, Tarucha S (2007) Micromagnets for coherent control of spin-charge qubit in lateral quantum dots. *Appl Phys Lett* 90(2):024105–024105-3.
21. Pioro-Ladrière M, et al. (2008) Electrically driven single-electron spin resonance in a slanting Zeeman field. *Nat Phys* 4(10):776–779.
22. Petta JR, Lu H, Gossard AC (2010) A coherent beam splitter for electronic spin states. *Science* 327(5966):669–672.
23. Prance JR, et al. (2012) Single-shot measurement of triplet-singlet relaxation in a Si/SiGe double quantum dot. *Phys Rev Lett* 108(4):046808.
24. Shi Z, et al. (2012) Fast hybrid silicon double-quantum-dot qubit. *Phys Rev Lett* 108(14):140503.
25. Shevchenko SN, Ashhab S, Nori F (2010) Landau–Zener–Stückelberg interferometry. *Phys Rep* 492(1):1–30.
26. Ribeiro H, Petta JR, Burkard G (2013) Interplay of charge and spin coherence in Landau-Zener-Stückelberg-Majorana interferometry. *Phys Rev B* 87(23):235318.
27. Cao G, et al. (2013) Ultrafast universal quantum control of a quantum-dot charge qubit using Landau-Zener-Stückelberg interference. *Nat Commun* 4:1401.
28. Granger G, et al. (2014) The visibility study of ST$_+$ Landau-Zener-Stückelberg oscillations without applied initialization. arXiv:1404.3636.
29. Assali LVC, et al. (2011) Hyperfine interactions in silicon quantum dots. *Phys Rev B* 83(16):165301.
30. Petersson KD, Petta JR, Lu H, Gossard AC (2010) Quantum coherence in a one-electron semiconductor charge qubit. *Phys Rev Lett* 105(24):246804.
31. Beaudoin F, Coish WA (2013) Enhanced hyperfine-induced spin dephasing in a magnetic-field gradient. *Phys Rev B* 88(8):085320.
32. Shi Z, et al. (2013) Coherent quantum oscillations and echo measurements of a Si charge qubit. *Phys Rev B* 88(7):075416.
33. Taylor JM, et al. (2007) Relaxation, dephasing, and quantum control of electron spins in double quantum dots. *Phys Rev B* 76(3):035315.
34. Culcer D, Zimmerman NM (2013) Dephasing of Si singlet-triplet qubits due to charge and spin defects. *Appl Phys Lett* 102(23):232108.
35. Morton JJ, McCamey DR, Eriksson MA, Lyon SA (2011) Embracing the quantum limit in silicon computing. *Nature* 479(7373):345–353.
36. Pla JJ, et al. (2012) A single-atom electron spin qubit in silicon. *Nature* 489(7417):541–545.
37. Büch H, Mahapatra S, Rahman R, Morello A, Simmons MY (2013) Spin readout and addressability of phosphorus-donor clusters in silicon. *Nat Commun* 4:2017.
38. Yin C, et al. (2013) Optical addressing of an individual erbium ion in silicon. *Nature* 497(7447):91–94.
39. Nordberg EP, et al. (2009) Enhancement-mode double-top-gated metal-oxide-semiconductor nanostructures with tunable lateral geometry. *Phys Rev B* 80(11):115331.
40. Lim WH, et al. (2009) Observation of the single-electron regime in a highly tunable silicon quantum dot. *Appl Phys Lett* 95(24):242102.
41. Xiao M, House MG, Jiang HW (2010) Measurement of the spin relaxation time of single electrons in a silicon metal-oxide-semiconductor-based quantum dot. *Phys Rev Lett* 104(9):096801.
42. Borselli MG, et al. (2011) Pauli spin blockade in undoped Si/SiGe two-electron double quantum dots. *Appl Phys Lett* 99(6):063109.
43. Ward DR, Savage DE, Lagally MG, Coppersmith SN, Eriksson MA (2013) Integration of on-chip field-effect transistor switches with dopantless Si/SiGe quantum dots for high-throughput testing. *Appl Phys Lett* 102(21):213107.
44. Eriksson MA, Coppersmith SN, Lagally MG (2013) Semiconductor quantum dot qubits. *MRS Bull* 38(10):794.
45. Simmons CB, et al. (2009) Charge sensing and controllable tunnel coupling in a Si/SiGe double quantum dot. *Nano Lett* 9(9):3234–3238.